

CLEAR-Mamba: Towards Accurate, Adaptive and Trustworthy Multi-Sequence Ophthalmic Angiography Classification

**Zhuonan Wang^{1*}, Wenjie Yan^{1*}, Wenqiao Zhang¹, Xiaohui Song^{1,2},
Jian Ma^{1,2}, Ke Yao^{1,2}, Yibo Yu^{1,2†}, Beng Chin Ooi¹**

¹Zhejiang University, ²Eye Center of the Second Affiliated Hospital

{wnzz, 22551068, wenqiaozhang, 2317050, jian_ma, xlren, yuyibo, ooibc}@zju.edu.cn

Abstract

Medical image classification is a core task in computer-aided diagnosis (CAD), playing a pivotal role in early disease detection, treatment planning, and patient prognosis assessment. In ophthalmic practice, fluorescein fundus angiography (FFA) and indocyanine green angiography (ICGA) provide hemodynamic and lesion-structural information that conventional fundus photography cannot capture. However, due to the single-modality nature, subtle lesion patterns, and significant inter-device variability, existing methods still face limitations in generalization and high-confidence prediction. To address these challenges, we propose ***CLEAR-Mamba***, an enhanced framework built upon MedMamba with optimizations in both architecture and training strategy. Architecturally, we introduce **HaC**, a hypernetwork-based adaptive conditioning layer that dynamically generates parameters according to input feature distributions, thereby improving cross-domain adaptability. From a training perspective, we develop **RaP**, a reliability-aware prediction scheme built upon evidential uncertainty learning, which encourages the model to emphasize low-confidence samples and improves overall stability and reliability. We further construct a large-scale ophthalmic angiography dataset covering both FFA and ICGA modalities, comprising multiple retinal disease categories for model training and evaluation. Experimental results demonstrate that ***CLEAR-Mamba*** consistently outperforms multiple baseline models, including the original MedMamba, across various metrics—showing particular advantages in multi-disease classification and reliability-aware prediction. This study provides an effective solution that balances generalizability and reliability for modality-specific medical image classification tasks.

Introduction

Recent advances in multimodal foundation models, driven by representation learning and large-scale pretraining, have enabled unified perception and reasoning across vision, language, and domain knowledge, demonstrating strong generalization across diverse applications. (Lin et al. 2025; Xie et al. 2025; Li et al. 2025; Zhang et al. 2022; Yuan et al. 2025b,a). Medical image classification is a fundamental task in computer-aided diagnosis (CAD), aiming to

automatically recognize disease types or pathological conditions from imaging data. With recent advances in deep learning, it has shown strong potential across diverse clinical scenarios (Dao and Ly 2025; Tang et al. 2022). Among imaging modalities, ophthalmic angiography is particularly important. FFA and ICGA provide dynamic cues of retinal hemodynamics and choroidal structures, supporting the diagnosis of diseases such as AMD (Wong et al. 2014), DR (Sivaprasad et al. 2012), and glaucoma (Thylefors and Negrel 1994). Compared with fundus photography, angiography better reveals subtle vascular abnormalities, offering richer evidence for diagnosis and treatment planning (Li et al. 2022; Mahendradas et al. 2021; Invernizzi et al. 2023).

The temporal nature of angiography offers unique opportunities for automated classification. However, most existing studies mainly focus on multimodal fusion (Luo et al. 2025; Yuan et al. 2025a,b). Typical CNN/ViT-based models integrate features from multiple modalities (e.g., CFP, OCT, OCTA, and FFA) to improve performance on AMD, glaucoma, and DR-related tasks. For instance, (Jin et al. 2022) fuses OCT and OCTA features to assess CNV activity, while MMRAF (Zhou et al. 2023) enhances glaucoma recognition via contrastive alignment, multi-instance representation, and hierarchical attention fusion. In addition, (Hervella et al. 2022) proposes cross-modal pretraining on unlabeled retinal image pairs to improve generalization.

While multimodal methods exploit complementary cues across modalities, they largely emphasize inter-modality integration. In contrast, a single FFA/ICGA exam naturally forms a sequential series of frames that captures hemodynamics and lesion evolution. Treating angiography as static images can miss temporal signatures (e.g., early filling to late leakage), thus underutilizing the diagnostic value of single-modality angiography. Meanwhile, mainstream architectures have inherent drawbacks for temporal imaging. CNNs struggle to capture long-range temporal dependencies due to limited receptive fields (Liu et al. 2024), whereas ViTs model global context at the cost of heavy computation and memory (Li et al. 2023), limiting real-time and resource-efficient deployment. Together with the underuse of angiography’s temporal dynamics, these issues remain a key bottleneck for clinically practical angiographic classification.

Beyond temporal modeling, medical AI systems also face two key bottlenecks: limited predictive reliability and weak

* These authors contributed equally.

† Corresponding author.

generalizability (Hasani et al. 2022; Zhang et al. 2024b). For reliability, softmax scores are often misused as confidence, leading to overconfident predictions on noisy or out-of-distribution inputs (Guo et al. 2017) and failing to disentangle epistemic and aleatoric uncertainty (Kendall and Gal 2017). In high-stakes settings, this can produce confident yet unreliable decisions, motivating standardized and quantifiable confidence estimation, e.g., calibration and uncertainty-aware deferral to human review when confidence is low. Equally important is generalizability. Many studies target single-disease classification (e.g., AMD, glaucoma, or DR), which often performs well in-domain but degrades in multi-disease or more complex clinical settings (Yang, Soltan, and Clifton 2022; Ong Ly et al. 2024). Recent efforts have explored parameter generation mechanisms to improve model adaptability without explicit fine-tuning, such as dynamically generating model parameters conditioned on domain or input characteristics (Lv et al. 2023). However, these approaches are primarily designed for device-level domain shifts and do not account for the temporal progression patterns or uncertainty-aware decision requirements inherent to ophthalmic angiography.

Taken together, conventional deep learning architectures and modeling paradigms remain inadequate for the comprehensive demands of ophthalmic angiography classification. Future methods must achieve breakthroughs in three core areas—making more effective use of temporal information, providing reliable confidence estimation, and enhancing adaptability across diverse clinical scenarios—before they can be truly translated into clinical practice.

To address these limitations, we propose ***CLEAR-Mamba*** for single-modality, multi-sequence angiography, aiming to improve temporal modeling, case adaptability, and prediction reliability. We curate a 43-disease dataset with complete FFA/ICGA sequences and adopt MedMamba as the backbone to efficiently capture long-range dynamics. We further introduce a HyperNetwork for lightweight, case-conditioned adaptation (Zhang et al. 2024a) and an evidential learning head to output calibrated predictions with uncertainty, enabling risk-aware deferral in ambiguous cases.

In summary, ***CLEAR-Mamba*** integrates large-scale multi-sequence angiography data, the efficient modeling capacity of the Mamba backbone, the adaptive representation of HyperNetworks, and the uncertainty quantification of evidential learning into a unified framework, offering a more robust and clinically oriented solution for angiographic image classification.

The main contributions are summarized as follows:

- **Method:** We propose ***CLEAR-Mamba***, built on MedMamba for efficient temporal modeling, augmented with a HyperNetwork for lightweight case-wise adaptation and evidential learning for calibrated confidence and uncertainty-aware predictions.
- **Dataset:** We curate a large-scale single-modality, multi-sequence FFA/ICGA dataset covering 43 diseases with complete temporal sequences to capture hemodynamics and lesion progression.
- **Results:** Extensive experiments on our dataset and public

benchmarks show consistent improvements over strong CNN/ViT/Mamba baselines (including MedMamba) in accuracy and reliability, demonstrating better temporal utilization, generalization, and confidence modeling.

Related Work

Medical Image Classification

Medical image classification (MIC) is a core task in computer-aided diagnosis, with deep learning substantially improving diagnostic accuracy and efficiency (Dao and Ly 2025). Early studies predominantly relied on CNNs (LeCun et al. 2002), while later works addressed robustness issues such as label noise (Liao et al. 2025). The introduction of Vision Transformers (ViTs) (Dosovitskiy et al. 2020) further advanced MIC by enhancing global representation modeling, leading to improved performance in complex modalities such as CT and MRI (Manzari et al. 2023). More recently, alternative backbones have been explored: MedMamba (Yue and Li 2024) leverages structured state space models (Gu 2023) to better handle long sequences. Despite these advances, most existing MIC methods remain single-modality and do not fully exploit multi-temporal characteristics, particularly in ophthalmic angiography. Meanwhile, growing clinical demands have motivated efforts toward better explainability and generalization (Rudin 2019; Van der Velden et al. 2022).

Ophthalmic Diagnostic Models

Recent ophthalmic diagnostic models increasingly exploit multimodal data (e.g., CFP, OCT, and angiography) to improve classification accuracy and generalization (Luo et al. 2025). Early studies mainly focused on single-disease scenarios, such as AMD (Chen et al. 2021), glaucoma (Mehta et al. 2021), and diabetic retinopathy (Hua et al. 2020), demonstrating that cross-modal attention and feature fusion can enhance disease-specific recognition. With growing demands for broader applicability, multi-disease classification has attracted increasing attention. Representative methods such as MSAN (He et al. 2021) employ region-guided and multi-scale attention to improve multimodal feature extraction, while EyeMoSt+ (Zou et al. 2024) further incorporates uncertainty modeling to enhance robustness under noisy conditions. Despite these advances, multimodal data are often unavailable in routine clinical practice, making single-modality settings more common. This highlights the importance of developing robust and generalizable single-modality models that can operate reliably under practical clinical constraints.

Ophthalmic Imaging Datasets

The development of ophthalmic AI models relies on high-quality and diverse datasets across modalities and disease categories (Luo et al. 2025). Early datasets mostly focused on single diseases, such as AREDS (Study et al. 1999) for AMD progression and DeepDRiD (Liu et al. 2022) for DR grading, with additional resources supporting glaucoma-related tasks. Later efforts expanded to limited multi-disease settings (e.g., Rabbani-I (Rasti et al. 2017) and

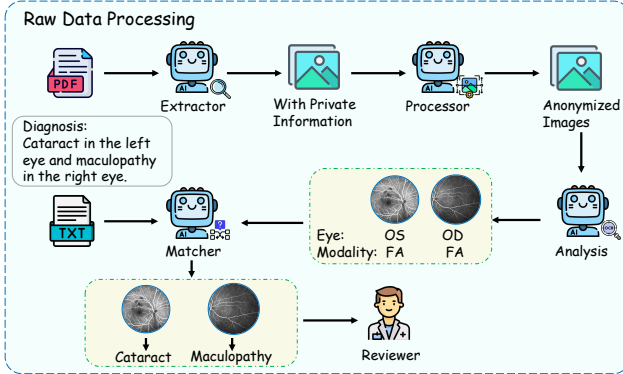


Figure 1: Automated pipeline for extracting, anonymizing, and aligning medical image–text data from raw PDF reports.

Messidor (Abràmoff et al. 2013)), and more recent datasets better reflect clinical diversity, including large-scale multi-pathology OCT collections (Kermany et al. 2018) and multi-modal resources such as BioMISA (Hassan et al. 2018) and ROSE (Ma et al. 2020). However, many datasets still suffer from class imbalance, annotation variability, and limited temporal coverage, which hinders robust and generalizable deployment in real-world clinics.

Data Collection and Processing

The dataset was collected from routine clinical case reports at a partner hospital, stored as PDFs containing multiple high-resolution angiography images with accompanying clinical text. It includes both structured attributes (e.g., demographics, exam metadata, modality, diagnosis) and unstructured content (images and narratives), covering FFA and ICGA across diverse retinal and choroidal disorders. As real-world data, it exhibits natural variability in acquisition quality.

Directly using the raw reports for training is challenging: images and text must be extracted and aligned from PDFs, privacy-sensitive identifiers must be removed, and label noise can arise from eye-level annotations within binocular images. Modality and laterality cues are also scattered across the report and require accurate parsing for correct image–label matching. To address this, we build an automated multi-agent pipeline (Fig. 1) to convert raw PDFs into a cleaned, structured dataset via extraction, anonymization, alignment, and mismatch filtering/re-annotation.

Multi-Agent Data Engine

We developed an multi-agent data processing engine that converts raw clinical PDF reports into high-quality structured image data. It performs document parsing, text extraction, image anonymization, lesion/label matching, and manual quality control in an end-to-end pipeline, with specialized agents collaborating to improve both efficiency and accuracy.

Extractor for Image Conversion Ophthalmic images are typically embedded in PDF examination reports, which are not directly usable for vision models. This module scans

PDFs page by page, detects image regions via layout analysis, and extracts them automatically. The images are then rendered as high-fidelity JPGs while preserving resolution and visual details, ensuring fine-grained lesion cues (e.g., edges and textures) are retained for downstream analysis.

Analyzer for Description Extraction To support lesion screening and label alignment, this module extracts key metadata from reports using OCR and NLP, including laterality (OS/OD) and modality (FFA/ICGA). It handles abbreviations and mixed Chinese–English writing via a standardized terminology dictionary and context-aware semantic matching. The parsed metadata are then bound to the corresponding images for downstream matching and classification.

Processor for Image Anonymization Ophthalmic images may contain identifiers (e.g., names, case IDs, dates) in edge overlays. This module automatically detects and masks/crops these regions using rule-based templates and detection models. To preserve diagnostic content, it first localizes retinal boundaries and avoids removing clinically relevant areas, while also cleaning residual device UI/backgrounds to produce privacy-safe images with retained diagnostic value.

Matcher for Binocular Lesion Screening Some reports include both eyes in a single image, making whole-image labels unreliable. Using extracted laterality/disease cues and fundus anatomical localization, this module verifies whether the diagnosis applies to one eye. If so, it splits the image into left/right regions, keeps the diagnosed eye, and discards or relabels the other as normal, reducing label noise and improving image–label consistency.

Reviewer for Quality Control To ensure research-grade quality, we add manual QC after automated processing. A stratified random subset is independently reviewed by at least two ophthalmologists for image clarity, anonymization correctness, and image–label consistency. Disagreements are adjudicated by a senior expert, and corrected labels are fed back to improve the pipeline.

Through the collaborative operation of these agents, we achieve a complete processing chain from raw PDF reports to standardized, high-quality ophthalmic classification data. This pipeline not only significantly reduces the workload and error rate of manual curation but also ensures consistency in visual quality, privacy protection, and label accuracy through multi-level validation and quality control.

Data Statistics

The final processed dataset consists of 15,524 valid pictures obtained from two angiographic modalities, representing 43 ocular illness categories and one healthy control group. For model construction, the dataset was divided at the patient level into training and test subsets in an approximate 80%:20% ratio. To guarantee that the disease categories and imaging modalities were distributed similarly across both subsets, a stratified sampling approach was used.

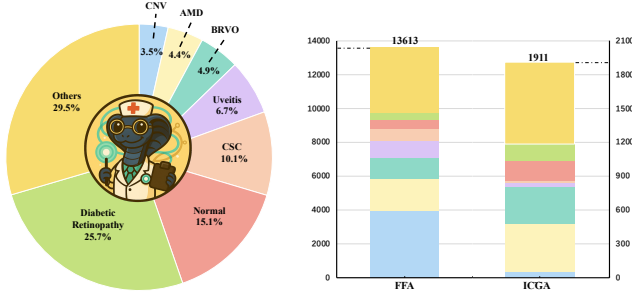


Figure 2: Dataset statistics. (a) Class distribution across 43 ocular categories showing a long-tailed pattern. (b) Modality proportion between FFA and ICGA images.

Data Distribution and Class Imbalance The dataset exhibits a pronounced long-tailed class distribution, typical of real-world clinical data. Diabetic Retinopathy (DR) is the largest class, with 3,990 photos (25.7%), followed by Normal (2,338), Central Serous Chorioretinopathy (CSC, 1,572), and Uveitis (1,036). Together, these high-frequency disorders account for the bulk of samples. Several categories, however, have fewer than 50 photos, including Punctate Inner Choroidopathy (PIC), Familial Exudative Vitreoretinopathy (FEVR), and Cataract.

This imbalance stems from two factors: (i) true clinical rarity (e.g., PIC and FEVR), which yields few angiographic records, and (ii) imaging-pathway bias, where some common conditions are seldom examined with FFA/ICGA (e.g., cataract, typically diagnosed via slit-lamp). These factors jointly produce a long-tailed distribution. We preserve this real-world skew for realistic evaluation, although it increases training difficulty by biasing models toward majority classes.

Imaging Modality Analysis The dataset includes two main angiographic modalities: fundus fluorescein angiography (FFA) and Indocyanine Green Angiography (ICGA). A total of 13,613 FFA photos (87.7%) and 1,911 ICGA images (12.3%) were obtained, demonstrating that FFA is still the predominate modality in clinical practice. Most retinal vascular and inflammatory diseases—such as DR, RVO/BRVO/CRVO, and uveitis—are principally scanned with FFA, accounting for more than 95% of samples, because these disorders are characterised by retinal vascular leakage and perfusion deficits that fluorescein imaging can detect. In contrast, choroidal and neovascular diseases (e.g., PCV, CNV, and choroidal masses) rely more heavily on ICGA, with proportions typically ranging from 25% to 50%, corresponding with clinical usage of ICGA to visualise deep choroidal circulation and neovascular complexes.

Method

In this section, we describe the design of **CLEAR-Mamba**. We first briefly review the key technical components relevant to angiography classification—efficient spatio-temporal backbones, conditional adaptation, and uncertainty-aware prediction—which form the basis of our framework. We then present **CLEAR-Mamba** and explain

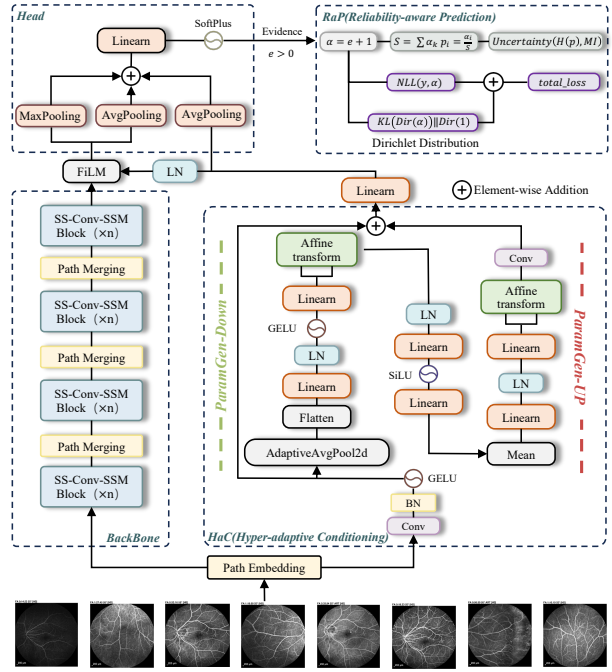


Figure 3: CLEAR-Mamba Framework.

how these components are integrated to meet the requirements of ophthalmic angiography classification.

Preliminaries

Before presenting **CLEAR-Mamba**, we briefly review three building blocks: MedMamba as an efficient SSM-based backbone for capturing local and long-range dependencies, HyperNetworks for lightweight instance-specific adaptation, and Evidential Learning for probabilistic prediction with calibrated uncertainty. Together, they form the basis of our method.

Medmamba MedMamba adopts visual state space models (VSSMs) to model long-range dependencies with linear complexity. It uses the 2D selective scan (SS2D) to efficiently propagate information over 2D feature maps, and employs a lightweight gate to fuse scanned features with the original representation.

Given an input image x' , patch embeddings are

$$X^{(0)} = \text{PatchEmbed}(x') \in \mathbb{R}^{B \times H' \times W' \times D}. \quad (1)$$

For each block $\ell = 0, \dots, L-1$, SS2D produces global-context features and the gate performs residual fusion:

$$Y^{(\ell)} = \text{SS2D}(X^{(\ell)}), \quad X^{(\ell+1)} = \text{Gate}([X^{(\ell)}, Y^{(\ell)}]) + X^{(\ell)}. \quad (2)$$

The final representation is obtained by global average pooling:

$$z = \text{GAP}(\text{NHWC} \rightarrow \text{NCHW}(X^{(L)})). \quad (3)$$

This backbone captures both fine-grained local cues and global structural dependencies, which is crucial for angiography images.

Experiment	Epochs	Batch	Opt.	LR	KL Coef	KL Scale
Primary (Ours)	150	128	Adam	10^{-3}	5×10^{-3}	1.2
RetinaMNIST	100	96	Adam	10^{-3}	5×10^{-3}	1.2
OCT-C8	20	32	Adam	10^{-3}	5×10^{-3}	1.2
Harvard-GDP	30	32	Adam	10^{-3}	5×10^{-3}	1.2

Table 1: Training hyperparameters on our in-house dataset (Primary) and public benchmarks. LR: learning rate; Opt.: optimizer; KL Coef/Scale: coefficient and scaling for the evidential KL term.

HyperNetwork A HyperNetwork conditions model parameters on an input z :

$$\theta = H_\psi(z), \quad y = F_\theta(x), \quad (4)$$

thus enabling instance-specific adaptation.

A lightweight form is FiLM, where G_ψ predicts feature-wise affine factors:

$$(\gamma, \beta) = G_\psi(z), \quad \tilde{X} = \gamma \odot X + \beta. \quad (5)$$

For higher capacity, the hypernetwork can generate (low-rank) adapter parameters:

$$h_\downarrow = \phi(W_\downarrow h + b_\downarrow), \quad \tilde{h} = h + W_\uparrow h_\downarrow + b_\uparrow. \quad (6)$$

We further apply a conditioned gate $\alpha = \sigma(a(z))$ to stabilize the update:

$$X_{\text{out}} = X + \alpha \odot (\tilde{X} - X). \quad (7)$$

FiLM is parameter-efficient, while adapter-based hypernetworks provide stronger conditional capacity.

Evidential Learning Evidential Deep Learning (EDL) models class probabilities with a Dirichlet distribution to provide both prediction and uncertainty. Given features z , the head outputs non-negative evidence:

$$e = \text{Softplus}(Wz + b), \quad \alpha = e + \mathbf{1}, \quad \hat{p}_k = \frac{\alpha_k}{\sum_{j=1}^K \alpha_j}. \quad (8)$$

Training combines likelihood with a Dirichlet prior regularizer:

$$\mathcal{L} = \mathcal{L}_{\text{NLL}}(\alpha; y) + \lambda \text{KL}[\text{Dir}(\alpha) \parallel \text{Dir}(\mathbf{1})]. \quad (9)$$

At inference, uncertainty can be summarized by predictive entropy $H(\hat{\mathbf{p}})$ and total evidence $S = \sum_k \alpha_k$ (larger S indicates lower epistemic uncertainty).

CLEAR-Mamba

We propose **CLEAR-Mamba**, a reliability-enhanced adaptive framework built on MedMamba. It follows an *encode-adapt-predict* pipeline: MedMamba encodes the input into hierarchical features, a lightweight adaptive modulation module applies sample-specific calibration, and an evidential classification head outputs both class probabilities and uncertainty. This design supports high-resolution angiography classification with strong adaptability and reliable uncertainty estimation.

Formally, let $X^{(L)}$ denote the backbone output. **CLEAR-Mamba** applies adaptive modulation:

$$\tilde{X}^{(L)} = X^{(L)} \odot \text{scale} + \text{shift}, \quad (10)$$

and then feeds $\tilde{X}^{(L)}$ into an evidential classifier that parameterizes a Dirichlet distribution:

$$\alpha = e + \mathbf{1}, \quad S = \sum_{k=1}^K \alpha_k, \quad \hat{p}_k = \frac{\alpha_k}{S}. \quad (11)$$

Hyper-adaptive Conditioning A HyperNetwork conditions model parameters on an input z :

$$\theta = H_\psi(z), \quad y = F_\theta(x), \quad (12)$$

thus enabling instance-specific adaptation.

A lightweight form is FiLM, where G_ψ predicts feature-wise affine factors:

$$(\gamma, \beta) = G_\psi(z), \quad \tilde{X} = \gamma \odot X + \beta. \quad (13)$$

For higher capacity, the hypernetwork can generate (low-rank) adapter parameters:

$$h_\downarrow = \phi(W_\downarrow h + b_\downarrow), \quad \tilde{h} = h + W_\uparrow h_\downarrow + b_\uparrow. \quad (14)$$

We further apply a conditioned gate $\alpha = \sigma(a(z))$ to stabilize the update:

$$X_{\text{out}} = X + \alpha \odot (\tilde{X} - X). \quad (15)$$

FiLM is parameter-efficient, while adapter-based hypernetworks provide stronger conditional capacity.

Reliability-aware Prediction To endow **CLEAR-Mamba** with reliable decision making, we integrate the evidential formulation (see Sec.) into the final classifier. Instead of outputting deterministic logits, the **RaP** head produces Dirichlet parameters α from the backbone features, yielding both class probabilities and an associated measure of uncertainty.

During training, we adopt the evidential objective introduced in Preliminaries, i.e., the marginal likelihood with a KL regularizer toward the non-informative prior $\text{Dir}(1)$. This encourages the model to express uncertainty when evidence is insufficient.

At inference, the **RaP** head outputs calibrated probabilities $\hat{\mathbf{p}}$ as well as uncertainty summaries. A key metric is the predictive entropy

$$H(\hat{\mathbf{p}}) = - \sum_{k=1}^K \hat{p}_k \log \hat{p}_k, \quad (16)$$

which grows when the prediction is uncertain. These scores provide a practical basis for selective review and risk-aware deployment in clinical settings.

Experiment

This section evaluates **CLEAR-Mamba** for ophthalmic image classification. We first describe the setup (datasets, metrics, and tuned hyper-parameters), then compare with baselines and assess robustness across datasets, followed by results and analysis.

Type	Model	Para. (M)	P(%)↑	Se(%)↑	Sp(%)↑	F1(%)↑	OA(%)↑	AUC↑
General Model	ResNet18(28)	34	7.77	7.18	98.31	6.52	39.08	0.7389
	ResNet18(224)	34	18.01	14.41	98.71	14.01	51.67	0.8633
	ResNet50(28)	71	4.41	5.22	98.15	4.16	35.65	0.6795
	ResNet50(224)	71	18.94	15.05	98.74	15.55	51.47	0.8596
	DINOv3-ViT-B	86	14.46	12.03	98.59	12.24	47.66	0.8176
	DINOv3-ViT-H+	840	10.91	8.87	98.44	8.72	42.66	0.7702
	DINOv3-ConvNeXt-B	89	14.79	11.10	98.56	11.24	46.83	0.8173
	DINOv3-ConvNeXt-L	198	15.69	11.25	98.61	10.96	46.93	0.8272
	MambaVision-T	150	7.56	6.37	98.33	5.34	41.48	0.7620
	MambaVision-S	95	10.33	8.65	98.53	7.74	46.57	0.8504
	MambaVision-B	292	9.57	9.17	98.53	8.26	46.76	0.8143
	MambaVision-L	684	10.94	8.45	98.49	7.67	45.8	0.8136
Medical Model	MedViT_V2_tiny	32	18.44	15.91	98.84	15.25	55.29	0.8784
	MedViT_V2_small	83	18.79	14.55	98.77	14.26	53.11	0.8632
	MedViT_V2_base	187	18.01	13.46	98.72	13.31	51.92	0.8595
	MedViT_V2_large	330	18.80	16.41	98.78	16.83	53.04	0.8647
	Medmamba-T	15	19.22	17.08	98.79	16.87	53.71	0.8714
	Medmamba-S	19	17.91	14.83	98.74	14.43	51.92	0.8614
	Medmamba-B	40	22.58	18.68	98.85	18.34	55.38	0.8790
	Medmamba-X	15	20.12	15.61	98.82	14.97	54.83	0.8833
	CLEAR-T	15	24.05	20.59	98.94	20.45	59.26	0.8450
	CLEAR-S	19	24.52	21.54	98.94	20.85	58.97	0.8590
	CLEAR-B	40	27.66	22.45	98.95	22.71	59.06	0.8360

Table 2: Quantitative comparison of general-purpose, medical-specific, and proposed models on the in-house angiography dataset. All models are trained and evaluated under identical experimental settings for fair comparison. The proposed **CLEAR-Mamba** framework is presented in three scales (*T/S/B*); for convenience, it is referred to as **CLEAR** in the following analysis.

Implementation details

All experiments were implemented in PyTorch 2.8 and run on a single NVIDIA GeForce RTX 5090 GPU. For public datasets, we followed the official preprocessing/protocols, and trained baselines with their default settings. **CLEAR-Mamba** used the hyperparameters in Table 1; otherwise, we keep a unified default configuration.

Specifically, the **RaP** (Reliability-aware Prediction) module was operated in the *adaptive* mode, with a KL divergence coefficient of 5×10^{-3} and a scaling factor of 1.2. For the **HaC** (Hyper-adaptive Conditioning) module, we systematically explored two key parameters: the reduction ratio $\{1, 2, 4, 8\}$ and the hidden feature dimension $\{32, 64, 96, 128\}$, resulting in 16 experimental configurations to comprehensively assess their influence on performance.

Experimental Datasets

This study targets multi-disease classification on FFA/ICGA sequences, where public datasets are scarce. Most existing ophthalmic benchmarks focus on single-disease tasks (e.g., DR or glaucoma) due to data sensitivity and privacy constraints. We therefore construct an in-house multi-disease angiography dataset with temporal information covering 43 categories as our primary benchmark. To further evaluate robustness and generalization, we also test on several external single-disease datasets with related clinical settings,

described below.

RetinaMNIST RetinaMNIST is a MedMNIST subset (Yang, Shi, and Ni 2021) derived from DeepDRiD (Liu et al. 2022), containing 1,600 fundus images labeled into five diabetic retinopathy severity levels. Images are center-cropped and resized to 28×28 , with splits of 1,080/120/400 for train/val/test. The task is ordinal DR grading, and remains challenging due to fine-grained differences and imbalanced severity distribution.

Harvard-GDP Harvard-GDP is a subset of the Harvard Glaucoma Detection and Progression dataset (Luo et al. 2023), collected from 1,000 patients. Each sample is a 224×224 RNFL thickness (RNFLT) map derived from 3D OCT, labeled as glaucomatous vs. non-glaucomatous based on visual-field-verified diagnosis. Using the provided train/val/test protocol, this benchmark is challenging because class differences in RNFLT maps are often subtle.

OCT-C8 OCT-C8 (Subramanian et al. 2022) is a composite OCT B-scan dataset compiled from public sources (e.g., Kaggle and Open-ICPSR), with $\sim 24k$ images across eight classes (AMD, CNV, DRUSEN, DME, DR, MH, CSR, Normal). Images are resized to 224×224 and split 75%/15%/15% for train/val/test. It serves as a multi-class retinal OCT benchmark with high intra-class variability and subtle inter-class differences.

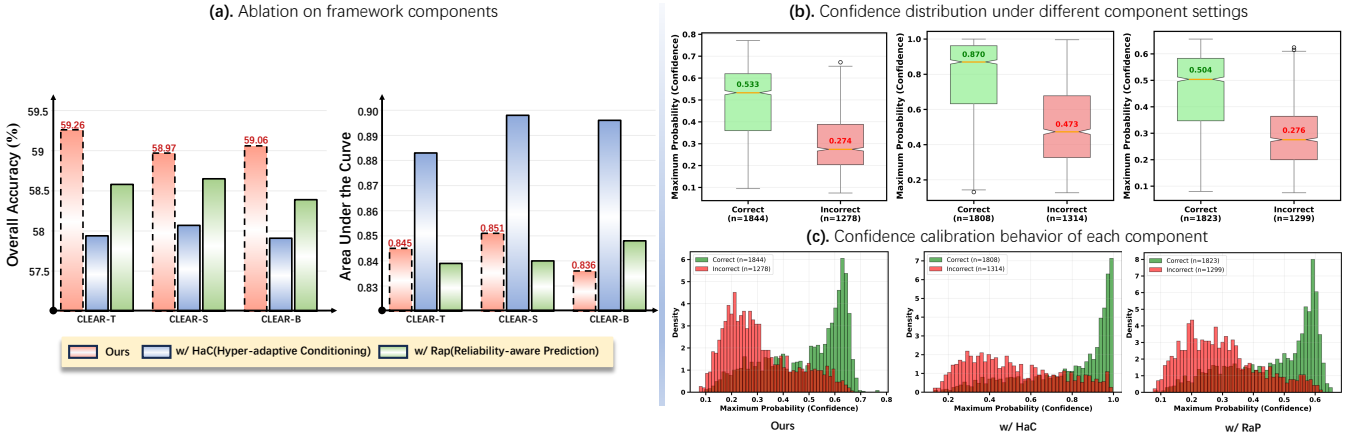


Figure 4: Component-level ablation study of the **CLEAR** framework. (a) Comparison of overall accuracy (OA) and AUC among different component configurations. (b) Boxplots and (c) density distributions of prediction confidence for correctly and incorrectly classified samples in different variants (**HaC**, **RaP**, and full model).

Evaluation Metrics

We consider a K -class classification problem on $\mathcal{D} = \{(x_i, y_i)\}_{i=1}^N$, where $y_i \in \{1, \dots, K\}$. The model outputs $\mathbf{p}_i \in [0, 1]^K$ and $\hat{y}_i = \arg \max_k p_{i,k}$. Let $\text{TP}_k, \text{FP}_k, \text{FN}_k, \text{TN}_k$ denote the confusion counts for class k .

We report Overall Accuracy (OA) and macro-averaged Precision, Sensitivity (Recall), Specificity, F1-score, and AUC. Specifically,

$$\text{OA} = \frac{\sum_{k=1}^K \text{TP}_k}{N}, \quad (17)$$

$$\text{Precision}_k = \frac{\text{TP}_k}{\text{TP}_k + \text{FP}_k}, \quad (18)$$

$$\text{Sensitivity}_k = \frac{\text{TP}_k}{\text{TP}_k + \text{FN}_k}, \quad (19)$$

$$\text{Specificity}_k = \frac{\text{TN}_k}{\text{TN}_k + \text{FP}_k}, \quad (20)$$

$$\text{F1}_k = \frac{2 \text{Precision}_k \text{Sensitivity}_k}{\text{Precision}_k + \text{Sensitivity}_k}. \quad (21)$$

Macro averages are computed as $\frac{1}{K} \sum_{k=1}^K (\cdot)$. AUC is computed in a one-vs-rest manner for each class and then macro-averaged.

In addition, we also analyzed the model’s computational complexity in terms of floating-point operations (FLOPs) and the total number of learnable parameters, providing a complementary view of efficiency alongside predictive performance.

Results on the In-house FFA/ICGA Dataset

We evaluate **CLEAR-Mamba** on our in-house multi-disease angiography dataset with full FFA/ICGA temporal sequences. This experiment tests its ability to model temporal hemodynamic cues and handle heterogeneous lesions. We further compare against representative CNN-, Transformer-, and Mamba-based baselines to assess reliability calibration and generalization under real-world clinical variability.

The Data We primarily evaluate **CLEAR-Mamba** on the test split of our in-house multi-disease angiography dataset, which serves as the main benchmark in this study. Detailed are provided in Sec. .

Preprocessing and Partitioning All FFA/ICGA frames were resized to 224×224 . During training, we applied random resized cropping and horizontal flipping, followed by normalization (mean/std = $(0.5, 0.5, 0.5)$). For validation, we used only resizing and normalization. We split the in-house dataset into 80%/20% for train/test. The best checkpoint was selected by validation OA and evaluated on the test set. For public datasets, we follow their official preprocessing and protocols for fair comparison.

Overall Comparison with Existing Models To comprehensively evaluate the discriminative capability and domain adaptability of our framework, we benchmarked the proposed **CLEAR-Mamba** models at three scales (T/S/B) under identical experimental settings. For simplicity, we use the term **CLEAR** to refer collectively to these variants in the following discussion.

As shown in Table 2, general-purpose backbones (e.g., ResNet, DINOv3, MambaVision) degrade substantially when trained from scratch on our angiography data. Their strong performance on natural images largely relies on large-scale pretraining; with random initialization and limited medical supervision, they struggle to capture fine-grained vascular textures and lesion cues. For instance, ResNet18(224) achieves 51.67% OA / 14.01% F1, and DINOv3-ViT-B obtains 47.66% OA / 12.24% F1. In contrast, medical-oriented models such as MedViT-V2 and MedMamba are more robust when trained from scratch. Their domain-aware designs (e.g., hierarchical fusion and context-preserving state-space modeling) provide stronger inductive bias, enabling effective learning on moderate-scale medical data. As a result, they achieve higher OA (51–55%) and F1 (13–18%) without large-scale pretraining.

Compared with MedViT-V2 and MedMamba, **CLEAR** achieves consistently higher sensitivity and OA across all

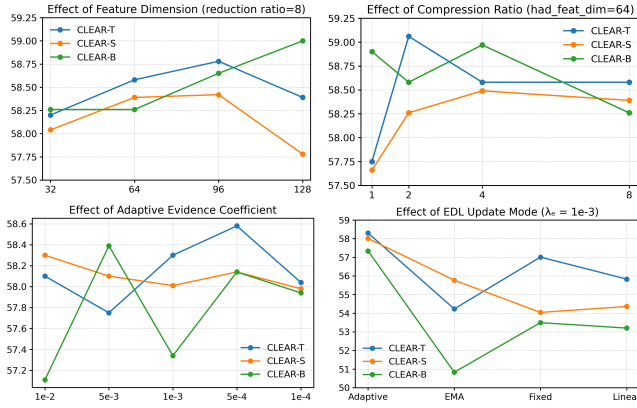


Figure 5: Hyperparameter-level ablation study of the **CLEAR** framework. Subfigures (a–d) are arranged clockwise from the top-left. (a) Effect of the hypernetwork feature dimension (`had_feat_dim`); (b) impact of the compression ratio (r); (c) sensitivity to the adaptive evidence coefficient (λ_e); and (d) comparison of EDL update strategies.

model scales. **CLEAR-T/S/B** obtain F1 scores of 20.45%, 20.85%, and 22.71%, with OA of 59.26%, 58.97%, and 59.06%, respectively, while maintaining high specificity (98.94–98.95%). Overall, CLEAR improves F1 by about +6–8 points and OA by about +4 points over MedMamba-X. We attribute these gains to **HaC** for instance-conditioned feature modulation and **RaP** for evidential uncertainty modeling, yielding more stable and calibrated predictions.

Ablation Study and Comparisons We conduct ablation studies to assess each component and hyperparameter effects. As shown in Fig. 4, the full model (“Ours”) achieves the best OA and AUC across scales. Both **HaC** and **RaP** improve performance, and combining them yields complementary gains.

Components Ablation. For clarity, we report **CLEAR-B** as a representative case (Fig. 4(b)–(c)), with similar trends on **CLEAR-T/S**. We observe three behaviors from the confidence distributions. **+HaC** is *overconfident*, assigning high confidence to both correct and incorrect predictions (median 0.870 vs. 0.473), which harms OA. **+RaP** is *overly conservative*, with confidence concentrated around ~ 0.6 even for easy cases. The full model achieves better calibration and separation, with median confidences of 0.533 (correct) and 0.274 (incorrect), yielding a larger confidence gap than **+RaP** and explaining its superior OA/AUC.

Impact of Hyperparameters. We analyze the sensitivity of **HaC** and **RaP** to key hyperparameters (Fig. 5), including `had_feat_dim`, the reduction ratio r , the evidential coefficient λ_e , and the EDL update strategy. For **HaC**, increasing `had_feat_dim` improves OA but quickly saturates (and may slightly drop) beyond 128, indicating diminishing returns and potential over-conditioning, especially for smaller variants (**CLEAR-T/S**); **CLEAR-B** benefits more but becomes slightly sensitive under stronger compression (higher r). For **RaP**, OA is stable across $\lambda_e \in [10^{-4}, 10^{-2}]$ (within $\sim 1\%$, Fig. 5(c)), while the *Adaptive* update consis-

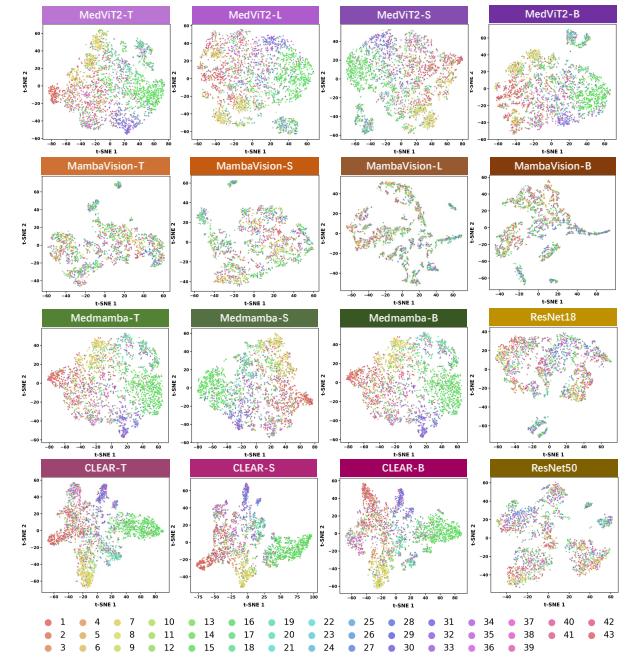


Figure 6: t-SNE visualization of feature embeddings from ResNet, MedViT2, MambaVision, MedMamba, and **CLEAR** on the in-house dataset.

tently yields the best results across scales (Fig. 5(d)), highlighting the value of dynamic evidence weighting for reliable uncertainty modeling.

In-depth Analysis Beyond feature separability, we further examine the reliability of model predictions by analyzing confidence and uncertainty under different ambiguity levels.

T-SNE Feature Visualization. We further visualize learned embeddings with t-SNE (Fig. 6). **CLEAR** shows tighter intra-class clustering and clearer inter-class separation than ResNet, MedViT, MambaVision, and MedMamba, even under the challenging 43-class setting. In contrast, other models exhibit more overlap, indicating weaker feature discriminability.

Confidence-Aware Reliability Analysis. We illustrate three samples with progressively increasing uncertainty. A confident and reliable prediction is observed for *BRVO*, characterized by a peaked distribution (top-1 = 0.63) and low uncertainty (Total Unc ≈ 1.84). For a *DR* sample, the prediction remains correct but becomes less decisive (top-1 = 0.40; others ≈ 0.10) with higher uncertainty (≈ 2.79), indicating that manual review may be needed. In a more ambiguous *uveitis* example, the model misclassifies it as *retinal hemorrhage* with low confidence (top-1 = 0.17) and high uncertainty (≈ 3.49), suggesting that **CLEAR** is aware of its unreliability rather than making an over-confident error.

Results on Public Datasets

Beyond our in-house angiography dataset, we evaluate cross-domain robustness on three public retinal benchmarks—RetinaMNIST, OCT-C8, and Harvard-GDP—covering fundus, OCT, and volumetric glaucoma

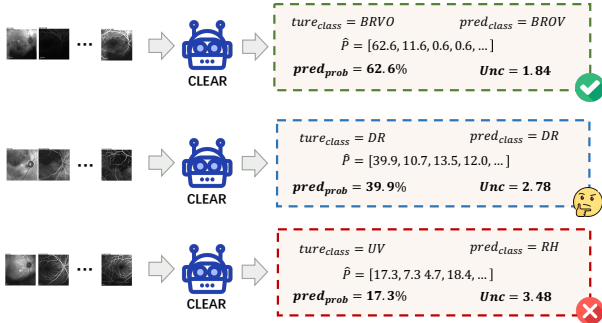


Figure 7: Case studies of the **RaP** module in **CLEAR**. Representative examples showing how quantifies uncertainty and adjusts confidence under different prediction scenarios: (a) confident and correct, (b) cautious but correct, and (c) prudent failure with high uncertainty.

Table 3: Performance comparison on the **Harvard-GDP** for the glaucoma **TD Progression forecasting** task. Values before and after the slash (“/”) indicate the results under **single-modality** and **multimodal fusion** settings, respectively.

Model	Acc↑	AUC↑
VGG	0.78/0.80	0.84/0.79
ResNet	0.75/0.74	0.74/0.75
ResNext	0.78/0.77	0.78/0.76
WideResNet	0.77/0.79	0.77/0.80
EfficientNet	0.73/0.78	0.76/0.79
ConvNext	0.74/0.81	0.78/0.81
ViT	0.73/0.77	0.68/0.79
Swin	0.71/0.77	0.68/0.77
CLEAR	0.91	0.85

data. These datasets allow us to assess whether **CLEAR-Mamba** maintains stable performance under domain shift and limited data, and to verify its scalability across input resolutions and label granularities without modifying the architecture or hyperparameters.

The Data The details of RetinaMNIST, Harvard-GDP, and OCT-C8 datasets are provided in Section .

Results on Public Retinal Datasets **Results on the Harvard-GDP.** Table 3 reports results on Harvard-GDP. Due to setting differences, we only compare the progression forecasting results with those reported in (Luo et al. 2023). As class imbalance reduces the sensitivity of metrics to model differences, we present results on the TD Progression task only and refer readers to (Luo et al. 2023) for full settings and additional results. Notably, **CLEAR** achieves state-of-the-art performance even with a single modality, outperforming all reported multimodal fusion models, suggesting strong progression cue modeling from OCT alone.

Results on the OCT-C8. Table 4 summarizes multi-class classification results on OCT-C8. Under the same protocol, **CLEAR** consistently improves OA and AUC. In particular, **CLEAR-S** achieves the best overall performance (94.5%

Table 4: Performance comparison on the **OCT-C8** dataset, which includes eight categories of retinal diseases (CNV, DME, DRUSEN, NORMAL, CSC, MH, AMD, and RVO).

Model	OA↑	AUC↑
DenseNet201	0.9214	—
VGG19	0.9018	—
InceptionV3	0.8675	—
CLEAR-T	0.9254	0.9918
CLEAR-S	0.9450	0.9961
CLEAR-B	0.9321	0.9934

Table 5: Performance comparison on the **RetinaMNIST**. Values indicate the overall accuracy (OA) and AUC on the test set.

Model	OA↑	AUC↑
ResNet18 (28)	52.4	0.717
ResNet18 (224)	49.3	0.710
ResNet50 (28)	52.8	0.726
ResNet50 (224)	51.1	0.716
Auto-sklearn	51.5	0.690
AutoKeras	50.3	0.719
Google AutoML	53.1	0.750
MedViT-T	53.4	0.752
MedViT-S	56.1	0.773
MedViT-L	55.2	0.754
MedMamba-T	54.3	0.747
MedMamba-S	54.5	0.718
MedMamba-B	55.3	0.715
CLEAR-T	55.8	0.738
CLEAR-S	56.5	0.729
CLEAR-B	56.8	0.742

OA, 0.9961 AUC), surpassing both CNN-based and hybrid medical vision baselines.

Results on the RetinaMNIST. Table 5 presents results on RetinaMNIST, where baselines are reproduced from the MedMamba paper. Under the same setting, **CLEAR** variants consistently outperform all baselines; **CLEAR-B** achieves the best accuracy (56.8%) and AUC (0.742), demonstrating robust generalization on retinal disease classification.

Conclusion

We proposed **CLEAR-Mamba**, a reliability-enhanced and adaptive framework for single-modality, multi-sequence ophthalmic angiography classification. It combines (1) a MedMamba backbone for efficient spatio-temporal modeling, (2) a Hyper-adaptive Conditioning (HaC) module for lightweight sample-wise adaptation, and (3) a Reliability-aware Prediction (RaP) head based on evidential learning to produce calibrated predictions with uncertainty estimates. We curate a large-scale angiography dataset covering 43 diseases with complete FFA/ICGA sequences, and evaluate our method both in-house and on three public benchmarks (Reti-

naMNIST, OCT-C8, and Harvard-GDP). CLEAR-Mamba consistently outperforms CNN/ViT/Mamba baselines in OA/F1/AUC, while exhibiting improved calibration and robustness under heterogeneous and imbalanced conditions, supporting its potential for trustworthy clinical use. Future work will focus on multi-center prospective validation, extending to multimodal fusion, integrating uncertainty with selective prediction and human-in-the-loop review, and exploring sequence-aware pretraining to further improve real-world generalization.

References

Abràmoff, M. D.; Folk, J. C.; Han, D. P.; Walker, J. D.; Williams, D. F.; Russell, S. R.; Massin, P.; Cochener, B.; Gain, P.; Tang, L.; et al. 2013. Automated analysis of retinal images for detection of referable diabetic retinopathy. *JAMA ophthalmology*, 131(3): 351–357.

Chen, Q.; Keenan, T. D.; Allot, A.; Peng, Y.; Agrón, E.; Domalpally, A.; Klaver, C. C.; Luttkhuizen, D. T.; Colyer, M. H.; Cukras, C. A.; et al. 2021. Multimodal, multi-task, multiattention (M3) deep learning detection of reticular pseudodrusen: Toward automated and accessible classification of age-related macular degeneration. *Journal of the American Medical Informatics Association*, 28(6): 1135–1148.

Dao, L.; and Ly, N. Q. 2025. Recent advances in medical image classification. *arXiv preprint arXiv:2506.04129*.

Dosovitskiy, A.; Beyer, L.; Kolesnikov, A.; Weissenborn, D.; Zhai, X.; Unterthiner, T.; Dehghani, M.; Minderer, M.; Heigold, G.; Gelly, S.; et al. 2020. An image is worth 16x16 words: Transformers for image recognition at scale. *arXiv preprint arXiv:2010.11929*.

Gu, A. 2023. *Modeling sequences with structured state spaces*. Stanford University.

Guo, C.; Pleiss, G.; Sun, Y.; and Weinberger, K. Q. 2017. On calibration of modern neural networks. In *International conference on machine learning*, 1321–1330. PMLR.

Hasani, N.; Morris, M. A.; Rhamim, A.; Summers, R. M.; Jones, E.; Siegel, E.; and Saboury, B. 2022. Trustworthy artificial intelligence in medical imaging. *PET clinics*, 17(1): 1.

Hassan, T.; Akram, M. U.; Masood, M. F.; and Yasin, U. 2018. BIOMISA retinal image database for macular and ocular syndromes. In *International Conference Image Analysis and Recognition*, 695–705. Springer.

He, X.; Deng, Y.; Fang, L.; and Peng, Q. 2021. Multi-modal retinal image classification with modality-specific attention network. *IEEE transactions on medical imaging*, 40(6): 1591–1602.

Hervella, A. S.; Rouco, J.; Novo, J.; and Ortega, M. 2022. Multimodal image encoding pre-training for diabetic retinopathy grading. *Computers in Biology and Medicine*, 143: 105302.

Hua, C.-H.; Kim, K.; Huynh-The, T.; You, J. I.; Yu, S.-Y.; Le-Tien, T.; Bae, S.-H.; and Lee, S. 2020. Convolutional network with twofold feature augmentation for diabetic retinopathy recognition from multi-modal images. *IEEE Journal of Biomedical and Health Informatics*, 25(7): 2686–2697.

Invernizzi, A.; Carreño, E.; Pichi, F.; Munk, M. R.; Agarwal, A.; Zierhut, M.; and Pavesio, C. 2023. Experts Opinion: OCTA vs. FFA/ICG in Uveitis—Which Will Survive? “Ten questions to find one answer”. *Ocular Immunology and Inflammation*, 31(8): 1561–1568.

Jin, K.; Yan, Y.; Chen, M.; Wang, J.; Pan, X.; Liu, X.; Liu, M.; Lou, L.; Wang, Y.; and Ye, J. 2022. Multimodal deep learning with feature level fusion for identification of choroidal neovascularization activity in age-related macular degeneration. *Acta Ophthalmologica*, 100(2): e512–e520.

Kendall, A.; and Gal, Y. 2017. What uncertainties do we need in bayesian deep learning for computer vision? *Advances in neural information processing systems*, 30.

Kermany, D. S.; Goldbaum, M.; Cai, W.; Valentim, C. C.; Liang, H.; Baxter, S. L.; McKeown, A.; Yang, G.; Wu, X.; Yan, F.; et al. 2018. Identifying medical diagnoses and treatable diseases by image-based deep learning. *cell*, 172(5): 1122–1131.

LeCun, Y.; Bottou, L.; Bengio, Y.; and Haffner, P. 2002. Gradient-based learning applied to document recognition. *Proceedings of the IEEE*, 86(11): 2278–2324.

Li, J.; Chen, J.; Tang, Y.; Wang, C.; Landman, B. A.; and Zhou, S. K. 2023. Transforming medical imaging with Transformers? A comparative review of key properties, current progresses, and future perspectives. *Medical image analysis*, 85: 102762.

Li, S.; Lin, T.; Lin, L.; Zhang, W.; Liu, J.; Yang, X.; Li, J.; He, Y.; Song, X.; Xiao, J.; et al. 2025. Eyecaregpt: Boosting comprehensive ophthalmology understanding with tailored dataset, benchmark and model. In *Proceedings of the 33rd ACM International Conference on Multimedia*, 3893–3902.

Li, X.-Y.; Wang, S.; Dong, L.; and Zhang, H. 2022. Comparison of fundus fluorescein angiography and fundus photography grading criteria for early diabetic retinopathy. *International Journal of Ophthalmology*, 15(2): 261.

Liao, Z.; Hu, S.; Zhang, Y.; and Xia, Y. 2025. Unleashing the potential of open-set noisy samples against label noise for medical image classification. *Medical Image Analysis*, 103702.

Lin, T.; Zhang, W.; Li, S.; Yuan, Y.; Yu, B.; Li, H.; He, W.; Jiang, H.; Li, M.; Song, X.; et al. 2025. Healthgpt: A medical large vision-language model for unifying comprehension and generation via heterogeneous knowledge adaptation. *arXiv preprint arXiv:2502.09838*.

Liu, R.; Wang, X.; Wu, Q.; Dai, L.; Fang, X.; Yan, T.; Son, J.; Tang, S.; Li, J.; Gao, Z.; et al. 2022. Deepdrid: Diabetic retinopathy—grading and image quality estimation challenge. *Patterns*, 3(6).

Liu, S.; Yue, W.; Guo, Z.; and Wang, L. 2024. Multi-branch CNN and grouping cascade attention for medical image classification. *Scientific Reports*, 14(1): 15013.

Luo, X.; Zheng, R.; Zheng, Q.; Du, Z.; Yang, S.; Ding, M.; Xu, Q.; Liu, C.; and Shen, L. 2025. A Survey of Multimodal Ophthalmic Diagnostics: From Task-Specific Approaches to Foundational Models. *arXiv preprint arXiv:2508.03734*.

Luo, Y.; Shi, M.; Tian, Y.; Elze, T.; and Wang, M. 2023. Harvard glaucoma detection and progression: A multi-modal multitask dataset and generalization-reinforced semi-supervised learning. In *Proceedings of the IEEE/CVF International Conference on Computer Vision*, 20471–20482.

Lv, Z.; Zhang, W.; Zhang, S.; Kuang, K.; Wang, F.; Wang, Y.; Chen, Z.; Shen, T.; Yang, H.; Ooi, B. C.; et al. 2023. Duet: A tuning-free device-cloud collaborative parameters generation framework for efficient device model generalization. In *Proceedings of the ACM Web Conference 2023*, 3077–3085.

Ma, Y.; Hao, H.; Xie, J.; Fu, H.; Zhang, J.; Yang, J.; Wang, Z.; Liu, J.; Zheng, Y.; and Zhao, Y. 2020. ROSE: a retinal OCT-angiography vessel segmentation dataset and new model. *IEEE transactions on medical imaging*, 40(3): 928–939.

Mahendradas, P.; Sridharan, A.; Kawali, A.; Sanjay, S.; and Venkatesh, R. 2021. Role of ocular imaging in diagnosis and determining response to therapeutic interventions in posterior and panuveitis. *The Asia-Pacific Journal of Ophthalmology*, 10(1): 74–86.

Manzari, O. N.; Ahmadabadi, H.; Kashiani, H.; Shokouhi, S. B.; and Ayatollahi, A. 2023. MedViT: a robust vision transformer for generalized medical image classification. *Computers in biology and medicine*, 157: 106791.

Mehta, P.; Petersen, C. A.; Wen, J. C.; Banitt, M. R.; Chen, P. P.; Bojikian, K. D.; Egan, C.; Lee, S.-I.; Balazinska, M.; Lee, A. Y.; et al. 2021. Automated detection of glaucoma with interpretable machine learning using clinical data and multimodal retinal images. *American Journal of Ophthalmology*, 231: 154–169.

Ong Ly, C.; Unnikrishnan, B.; Tadic, T.; Patel, T.; Duhamel, J.; Kandel, S.; Moayed, Y.; Brudno, M.; Hope, A.; Ross, H.; et al. 2024. Shortcut learning in medical AI hinders generalization: method for estimating AI model generalization without external data. *NPJ digital medicine*, 7(1): 124.

Rasti, R.; Rabbani, H.; Mehridehnavi, A.; and Hajizadeh, F. 2017. Macular OCT classification using a multi-scale convolutional neural network ensemble. *IEEE transactions on medical imaging*, 37(4): 1024–1034.

Rudin, C. 2019. Stop explaining black box machine learning models for high stakes decisions and use interpretable models instead. *Nature machine intelligence*, 1(5): 206–215.

Sivaprasad, S.; Gupta, B.; Crosby-Nwaobi, R.; and Evans, J. 2012. Prevalence of diabetic retinopathy in various ethnic groups: a worldwide perspective. *Survey of ophthalmology*, 57(4): 347–370.

Study, T. A.-R. E. D.; et al. 1999. The age-related eye disease study (AREDS): design implications AREDS report no. 1. *Controlled clinical trials*, 20(6): 573–600.

Subramanian, M.; Shanmugavadiel, K.; Naren, O. S.; Premkumar, K.; and Rankish, K. 2022. Classification of retinal oct images using deep learning. In *2022 international conference on computer communication and informatics (ICCCI)*, 1–7. IEEE.

Tang, P.; Yan, X.; Nan, Y.; Xiang, S.; Krammer, S.; and Lasser, T. 2022. FusionM4Net: A multi-stage multi-modal learning algorithm for multi-label skin lesion classification. *Medical Image Analysis*, 76: 102307.

Thylefors, B.; and Negrel, A. 1994. The global impact of glaucoma. *Bulletin of the World Health Organization*, 72(3): 323.

Van der Velden, B. H.; Kuijf, H. J.; Gilhuijs, K. G.; and Viergever, M. A. 2022. Explainable artificial intelligence (XAI) in deep learning-based medical image analysis. *Medical image analysis*, 79: 102470.

Wong, W. L.; Su, X.; Li, X.; Cheung, C. M. G.; Klein, R.; Cheng, C.-Y.; and Wong, T. Y. 2014. Global prevalence of age-related macular degeneration and disease burden projection for 2020 and 2040: a systematic review and meta-analysis. *The Lancet Global Health*, 2(2): e106–e116.

Xie, Y.; Li, S.; Lin, T.; Wang, Z.; Yang, C.; Zhong, Y.; Zhang, W.; Li, H.; Jiang, H.; Zhang, F.; et al. 2025. Heartcare Suite: Multi-dimensional Understanding of ECG with Raw Multi-lead Signal Modeling. *arXiv preprint arXiv:2506.05831*.

Yang, J.; Shi, R.; and Ni, B. 2021. Medmnist classification decathlon: A lightweight automl benchmark for medical image analysis. In *2021 IEEE 18th International Symposium on Biomedical Imaging (ISBI)*, 191–195. IEEE.

Yang, J.; Soltan, A. A.; and Clifton, D. A. 2022. Machine learning generalizability across healthcare settings: insights from multi-site COVID-19 screening. *NPJ digital medicine*, 5(1): 69.

Yuan, Y.; Zhang, H.; Li, W.; Cheng, Z.; Zhang, B.; Li, L.; Li, X.; Zhao, D.; Zhang, W.; Zhuang, Y.; et al. 2025a. Videorefer suite: Advancing spatial-temporal object understanding with video llm. In *Proceedings of the Computer Vision and Pattern Recognition Conference*, 18970–18980.

Yuan, Y.; Zhang, W.; Li, X.; Wang, S.; Li, K.; Li, W.; Xiao, J.; Zhang, L.; and Ooi, B. C. 2025b. PixelRefer: A Unified Framework for Spatio-Temporal Object Referring with Arbitrary Granularity. *arXiv preprint arXiv:2510.23603*.

Yue, Y.; and Li, Z. 2024. Medmamba: Vision mamba for medical image classification. *arXiv preprint arXiv:2403.03849*.

Zhang, W.; Lin, T.; Liu, J.; Shu, F.; Li, H.; Zhang, L.; Wanggui, H.; Zhou, H.; Lv, Z.; Jiang, H.; et al. 2024a. Hyperllava: Dynamic visual and language expert tuning for multimodal large language models. *arXiv preprint arXiv:2403.13447*.

Zhang, W.; Lv, Z.; Zhou, H.; Liu, J.-W.; Li, J.; Li, M.; Li, Y.; Zhang, D.; Zhuang, Y.; and Tang, S. 2024b. Revisiting the domain shift and sample uncertainty in multi-source active domain transfer. In *Proceedings of the IEEE/CVF Conference on Computer Vision and Pattern Recognition*, 16751–16761.

Zhang, W.; Zhu, L.; Hallinan, J.; Zhang, S.; Makmur, A.; Cai, Q.; and Ooi, B. C. 2022. Boostmis: Boosting medical image semi-supervised learning with adaptive pseudo labeling and informative active annotation. In *Proceedings of the IEEE/CVF conference on computer vision and pattern recognition*, 20666–20676.

Zhou, Y.; Yang, G.; Zhou, Y.; Ding, D.; and Zhao, J. 2023. Representation, alignment, fusion: A generic transformer-based framework for multi-modal glaucoma recognition. In *International Conference on Medical Image Computing and Computer-Assisted Intervention*, 704–713. Springer.

Zou, K.; Lin, T.; Han, Z.; Wang, M.; Yuan, X.; Chen, H.; Zhang, C.; Shen, X.; and Fu, H. 2024. Confidence-aware multi-modality learning for eye disease screening. *Medical Image Analysis*, 96: 103214.